Article

Numerical Modeling of Transient Two-Phase Flow and the Coalescence and Breakup of Bubbles in a Continuous Casting Mold

Yushi Tian [1,2], Pengzhao Shi [2], Lijun Xu [2,*], Shengtao Qiu [2] and Rong Zhu [1]

[1] School of Metallurgical and Ecological Engineering, University of Science and Technology Beijing, Beijing 100083, China; yushi_tian@tom.com (Y.T.); zhurong@ustb.edu.cn (R.Z.)

[2] National Engineering Research Center of Continuous Casting Technology, Central Iron and Steel Research Institute, Beijing 100081, China; shipengzhao1990@163.com (P.S.); qiust@vip.sina.com (S.Q.)

[*] Correspondence: ljxuah@sina.com; Tel.: +86-010-62182665

Abstract: The multiphase flow and spatial distribution of bubbles inside a continuous casting (CC) mold is a popular research issue due to its direct impact on the quality of the CC slab. The behavior of bubbles in the mold, and how they coalesce and break apart, have an important influence on the flow pattern and entrapment of bubbles. However, due to the limitations of experiments and measurement methods, it is impossible to directly observe the multiphase flow and bubble distribution during the CC process. Thus, a three-dimensional mathematical model which combined the large eddy simulation (LES) turbulent model, VOF multiphase model, and discrete phase model (DPM) was developed to study the transient two-phase flow and spatial distribution of bubbles in a continuous casting mold. The interaction between the liquid and bubbles and the coalescence, bounce, and breakup of bubbles were considered. The measured meniscus speed and bubble diameter were in good agreement with the measured results. The meniscus speed increased first and then decreased from the nozzle to the narrow face, with a maximum value of 0.07 m/s, and appeared at 1/4 the width of the mold. The current mathematical model successfully predicted the transient asymmetric two-phase flow and completely reproduced the coalescence, bounce, and breakup of bubbles in the mold. The breakup mainly occurred near the bottom of the submerged entry nozzle (SEN) due to the strong turbulent motion of the molten steel after hitting the bottom of the SEN. The average bubble diameter was about 0.6 mm near the nozzle and gradually decreased to 0.05 mm from the nozzle to the narrow face. The larger bubbles floated up near the SEN due to the effect of their greater buoyancy, while the small bubbles were distributed discretely in the entire mold with the action of the molten steel jet. Overall, the bubbles were distributed in a fan shape. The largest concentration of bubbles was in the lower part of the SEN and the upper edge of the SEN outlet.

Keywords: bubbles; spatial distribution; coalescence; bounce; breakup; continuous casting mold; large eddy simulation

1. Introduction

The argon injection method is widely used in the continuous casting (CC) process to prevent the clogging of the submerged entry nozzle (SEN) [1]. The injected discrete argon bubbles can effectively prevent the clogging of the SEN, but it is also a key factor for quality defects in steel products. The argon bubbles either move to the top slag layer to be removed from the molten steel, or they move to the solidification front to be captured as defects [2]. Therefore, the prediction of the motion and spatial distribution of bubbles in the mold is of great significance to improve the quality of CC slabs. Many scholars have carried out measurement studies on the distribution of bubbles in the SEN and mold [3–7], including the effect of the gas flow rate, the diameter of the injection port, the density of

the gas and liquid, and the surface tension. Cho [8] and Bai [3] studied the formation, expansion and growth, and breakup of bubbles under different injection methods using a mold water model. The above studies were carried out based on physical simulation, which has a definite gap with the distribution of bubbles under high temperature and high pressure during the actual CC process. The numerical simulation method can overcome these shortcomings, and it has therefore been widely developed and applied [9].

Yang [10] gave a detailed overview of the multiphase flow model applied in the CC process. The solution methods of multiphase flow are mainly divided into the Eulerian–Lagrangian model [11–13] and the Eulerian-Eulerian model [14–16]. Both the molten steel and argon bubbles were considered as a continuum phase, and the interaction between different phases was solved by the interphase force in the Eulerian-Eulerian model. Liu [17] used a Eulerian multiphase model to predict the time-dependent argon–steel–slag–air quasi-four-phase flow inside a slab CC mold. Three typical flow patterns inside the mold with different gas flow rates were proposed. Thomas [18,19] developed a coupled standard k-ε turbulence model and the Eulerian-Eulerian model to investigate the effect of argon gas bubble injection on flow-related phenomena in a typical steel slab caster. Àvila-Ortiz [20] developed a mathematical model to simulate the influence of the flow rate of the gas on the flow patterns of the liquid in a water–air model. Previous studies have mostly used the Eulerian-Eulerian model to simulate the multiphase flow in the mold, but the Eulerian-Eulerian model cannot provide individual information, such as the spatial distribution, velocity, and size of each bubble. The molten steel was treated as a continuum phase, and the argon bubbles were treated as a discrete phase in the Eulerian–Lagrangian model. The bubbles were tracked by solving their motion equations [21]. Using this model, Lei [22] developed a three-dimensional model to study the dynamic evolution of the gas–liquid interface and the solidification process. Chen [23–25] combined the large eddy simulation (LES) turbulent model, the VOF multiphase model, and the discrete phase model (DPM) to evaluate the effects of different interphase forces on the fluid flow and the spatial distribution of the bubbles in a CC strand. The bubble diameter was obtained by transforming the water model measurements through empirical formulas [26]. Wang [27] investigated the influence of the argon flow rate on the multiphase flow, heat transfer, and initial solidification in a CC slab mold. Although numerous results have been published, the vast majority of studies have ignored the interaction between bubbles, such as the coalescence and breakup of bubbles.

Many fundamental theories of bubble coalescence [28,29] and breakup [30,31] have been published. However, the behavior of the bubbles under the two-phase flow is such a complex phenomenon that there was and is no complete model applicable to all situations. In particular, the coalescence and breakup of bubbles in the continuous casting process of molten steel still needs further research. Based on the Eulerian-Eulerian model, Liu [32] used the k-ε model and the Multiple-Size-Group (MUSIG) model to predict the polydispersed bubble flow and bubble size distribution inside the slab CC mold. Santos [33] also employed the MUSIG model to discuss the effect of gas distribution on the flow field of liquid inside the mold and other metallurgical aspects. A relatively small number of studies using the Eulerian–Lagrangian model method to study the bubble diameter distribution have also been published. Zhang et al. [34,35] developed a new mathematical model considering the process of bubble interaction to simulate the fluid flow, dispersed bubble motion, and transport process in the slab CC mold. Using the modified bubble coalescence and breakup models, Yang [36,37] simulated bubble behavior in a slab CC mold. It found that the bubble size and number at both the narrow and wide faces decreased with the increase in distance from the meniscus. The effect of the initial bubble size on the distribution of bubbles captured by the solidification shell was also studied [38]. The above researchers have developed an understanding of the size distribution of bubbles in the mold to a certain extent. However, the effect of the transient asymmetric flow field in the CC mold on the bubble behavior was not considered. The transient asymmetric flow existing in the mold was indeed found to have a significant effect on the bubble distribution [39,40].

Therefore, our understanding of the interaction between the molten steel and the bubbles, and the interaction between the bubbles on the basis of the transient fluid flow, still need further study.

Therefore, in the current study, a three-dimensional mathematical model combining the LES turbulent model, VOF multiphase model, and DPM was established to study the two-phase flow and spatial distribution of bubbles in a CC mold. The transient asymmetric fluid flow and the coalescence, bounce, and breakup of bubbles were included to achieve an accurate prediction of the spatial distribution of bubbles.

2. Mathematical Formulation

2.1. Governing Equation

2.1.1. Turbulence Model

The transient turbulent fluid flow inside the SEN and the mold are resolved using the LES model. The governing equation of the momentum is defined as:

$$\frac{\partial}{\partial t}(\rho u_i) + \frac{\partial}{\partial x_j}(\rho u_i u_j) = -\frac{\partial p}{\partial x_i} + \frac{\partial}{\partial x_j}\left[(\mu + \mu_t)\left(\frac{\partial u_i}{\partial x_j} + \frac{\partial u_j}{\partial x_i}\right)\right] + F_{mom,i} \tag{1}$$

where ρ is the density in kg/m^3, t is the time in s; u is the velocity in m/s, p is the pressure in Pa, μ is the viscosity in kg/(m·s), and $F_{mom,i}$ is the source term induced by the interaction between bubbles and molten steel in kg/(m^2·s^2). The turbulent viscosity μ_t is calculated using the Smagorinsky–Lilly model [41], as shown in Equation (2).

$$\mu_t = \rho L_s^2 \sqrt{2\overline{S}_{ij}\overline{S}_{ij}} = \rho \left[\min\left(\kappa d, C_S V^{\frac{1}{3}}\right)\right]^2 \sqrt{2\overline{S}_{ij}\overline{S}_{ij}} \tag{2}$$

where κ is the Kármán constant; d is the distance to the closest wall in m; C_S is the Smagorinsky constant, and V is the volume of the computational cell in m^3. L_S is the mixing length for sub grid scales in m, and S is the rate-of-strain tensor for the resolved scale in s^{-1}.

2.1.2. Multiphase Model

The liquid water and air layer at the top of the mold are considered as a continuum phase. The interface between the water and air is tracked using the VOF multiphase model by the solution of a continuity equation for the volume fraction of each phase. For the phase q, the continuity equation is calculated as:

$$\frac{\partial}{\partial t}(\alpha_q \rho_q) + \nabla \cdot (\alpha_q \rho_q u_q) = 0 \tag{3}$$

where α_q is the volume fraction of phase q; u_q is the velocity of phase q in m/s.

2.1.3. Bubble Tracking Model

The bubbles inside the mold are treated as a discrete phase, and their motions are governed by integrating the force balance on the particle in a Lagrangian reference frame:

$$\frac{du_b}{dt} = F_b + F_D + F_L + F_P + F_{VM} \tag{4}$$

where the terms on the right side of the equation are gravity buoyancy force, drag force, lift force, pressure gradient force, and virtual mass force, respectively. The two-way coupled DPM is achieved by including those interphase forces between the water and bubbles. The effect of the lift force is calculated using a User-Defined Function (UDF).

The gravity buoyancy force is given by:

$$F_b = \frac{\rho_b - \rho_l}{\rho_b} g \tag{5}$$

where the ρ_b is the bubble density in kg·m^{-3}, and ρ_l is the water density in kg·m^{-3}.

The drag force is given by:

$$F_D = \frac{3}{4} \frac{\mu C_D \text{Re}}{\rho_b d^2} (u_l - u_b) \tag{6}$$

where C_D is the drag coefficient and calculated in Equation (7), μ is the viscosity of the liquid in kg·m^{-1}·s^{-1}, d is the bubble diameter in m, Re is the relative Reynolds number, u_l is the liquid velocity in m·s^{-1}, and u_b is the bubble velocity in m·s^{-1}.

$$\begin{cases} C_{Dvis} = \frac{24}{\text{Re}} \times \left(1 + 0.1 \times \text{Re}^{0.75}\right) & C_{Dvis} > C_{Ddis}, C_D = C_{Dvis} \\ C_{Ddis} = \frac{2}{3} \times \left(\frac{(g\rho_l)^{0.5} d}{\sigma^{0.5}}\right) \times \left(\frac{1 + 17.67(1 - \alpha_g)^{1.286}}{18.67(1 - \alpha_g)^{1.5}}\right) & C_{Dvis} < C_{Ddis} < C_{Dcap}, C_D = C_{Ddis} \\ C_{Dcap} = \frac{8}{3}(1 - a_g)^2 & C_{Ddis} > C_{Dcap}, C_D = C_{Dcap} \end{cases} \tag{7}$$

The lift force is given by:

$$F_L = C_L \frac{\rho_l}{\rho_b} (u_l - u_b) \times \nabla \times u_l \tag{8}$$

where C_L is the lift force coefficient and is calculated using the Tomiyama model [42] as follows:

$$C_L = \begin{cases} \text{Min}[0.288 \tan h(0.121\text{Re}, f(Eo'))] & \text{if } Eo' \le 4 \\ f(Eo') & \text{if } 4 < Eo' \le 10 \\ -0.27 & \text{if } 10 \le Eo' \end{cases}, \tag{9}$$

$$f\left(Eo'\right) = 0.00105\left(Eo'\right)^3 - 0.0159\left(Eo'\right)^2 - 0.0204 Eo' + 0.47 \tag{10}$$

$$Eo = \frac{g(\rho_l - \rho_b)d^2}{\sigma} \tag{11}$$

$$Eo' = \frac{g\left(\rho_l - \rho_g\right)\left(1 + 0.163 Eo^{0.757}\right)^{2/3} d^2}{\sigma} \tag{12}$$

The pressure gradient force is given by:

$$F_P = \frac{\rho_l}{\rho_b} u_b \nabla u_l \tag{13}$$

The virtual mass force is given by:

$$F_{VM} = C_{vm} \frac{\rho_l}{\rho_b} \left(u_b \nabla u_l - \frac{du_b}{dt}\right) \tag{14}$$

where C_{vm} is the virtual mass force coefficient and set as 0.5.

2.1.4. Coalescence, Bounce, and Breakup Model

The O'Rourke algorithm [43] is used to calculate the probability of the collision of two bubbles. When the bubble i center passes within a flat circle centered around the bubble j of area $\pi(r_i + r_j)^2$ perpendicular to the trajectory of the bubble i, a collision takes place. A collision volume to calculate the probability of collision in the O'Rourke algorithm is used, as shown in Equation (15).

$$V_c = \pi\left(r_i + r_j\right)^2 u_R \Delta t \tag{15}$$

where r_i and r_j are the radii of bubble i and bubble j, respectively; u_R is the relative velocity between the water and bubbles.

This assumes that there is a uniform probability of the bubble being anywhere within the cell, so the chance of the bubble being within the collision volume is the ratio of the two volumes. Thus, the probability of the bubble j colliding with bubble i is calculated as:

$$P = \frac{\pi (r_i + r_j)^2 u_R \Delta t}{V} \tag{16}$$

where V is the mesh volume where the bubble is located.

The outcome of the collision tends to be coalescence if the bubbles collide head-on, and bouncing if the collision is more oblique. The critical offset b_{crit} and the actual collision parameter b are proposed to determine the outcome of the collision [43]:

$$b = (r_i + r_j)\sqrt{Y} \tag{17}$$

$$b_{crit} = (r_i + r_j)\sqrt{\min\left(1.0, \frac{2.4f}{We}\right)} \tag{18}$$

$$f = \left(\frac{r_i}{r_j}\right)^3 - 2.4\left(\frac{r_i}{r_j}\right)^2 + 2.7\left(\frac{r_i}{r_j}\right)$$
$$We = \frac{\rho u_R^2 \sqrt{d_i d_j}}{\sigma} \tag{19}$$

where Y is a random number between 0 and 1.

Coalescence occurs when the critical offset b_{crit} is larger than the actual collision parameter b. The velocity and radius of the generated bubble are calculated in Equation (20). Otherwise, the new velocities are calculated in Equation (21) for the case of a grazing collision.

$$u_i' = \frac{m_i u_i + m_j u_j}{m_i + m_j}, r_i' = \left(\frac{3(m_i + m_j)}{4\pi\rho_b}\right)^{\frac{1}{3}} \tag{20}$$

$$u_i' = \frac{m_i u_i + m_j u_j}{m_i + m_j} + \frac{m_j u_R}{m_i + m_j}\left(\frac{b - b_{crit}}{r_i + r_j - b_{crit}}\right)$$
$$u_j' = \frac{m_i u_i + m_j u_j}{m_i + m_j} + \frac{m_i u_R}{m_i + m_j}\left(\frac{b - b_{crit}}{r_i + r_j - b_{crit}}\right) \tag{21}$$

where m_i and m_j are the masses of bubble i and bubble j, respectively; u_i and u_j are the velocities of bubble i and bubble j, respectively;

The strong turbulent flow in the SEN and the mold causes the breakup of bubbles. Therefore, there is a critical diameter for the stable existence of bubbles under different turbulent kinetic energies. Evans [44] proposes a maximum stable bubble size d_{crit} as:

$$d_{crit} = \left(\frac{We_c \sigma}{2\rho_l}\right)\varepsilon^{-0.4} \tag{22}$$

where We_c is the critical Weber number and set as 1.2; ε is the turbulent energy dissipation rate in m^2/s^3.

Breakup happens when the bubble diameter d_p is larger than d_{crit}. Then, the smaller daughter bubble size d_1 is randomly determined in the range of d_{min} and d_{max} determined by force balance criteria and mass balance criteria [45,46].

$$d_{min} = \frac{\sigma}{\rho_l \frac{u_\lambda^2}{2}} d_{max} = \frac{1}{\sqrt[3]{2}} d_p \tag{23}$$

where u_λ is the eddy velocity in m/s. Once d_1 is determined, another daughter bubble diameter d_2 is calculated by Equation (24).

$$d_2 = \left(d_p^3 - d_1^3\right)^{\frac{1}{3}} \tag{24}$$

2.2. Computational Domain and Computational Details

In the current study, a three-dimensional mathematical model based on a 1/4 scale water model of a slab CC mold was carried out. Figure 1 shows the distribution of the computational domain and mesh system. The mesh near the water–air interface was refined to accurately capture the distribution of the liquid level. The total number of meshes was about 440,000. The section size of the CC mold was 510 mm × 50 mm, and the thickness of the air layer at the top of the CC mold was 25 mm. The casting speed was 0.425 m/min. The air gas was injected at the inlet of the SEN, and the flow rate was 90 mL/min. More detailed model parameters and physical properties can be found elsewhere [23]. The three-dimensional transient two-phase flow in the SEN and the CC mold was simulated using the LES model and VOF model. The trajectories of gas bubbles were tracked using the DPM. The interaction between the liquid and bubbles and the coalescence, bounce, and breakup of bubbles were included using a UDF.
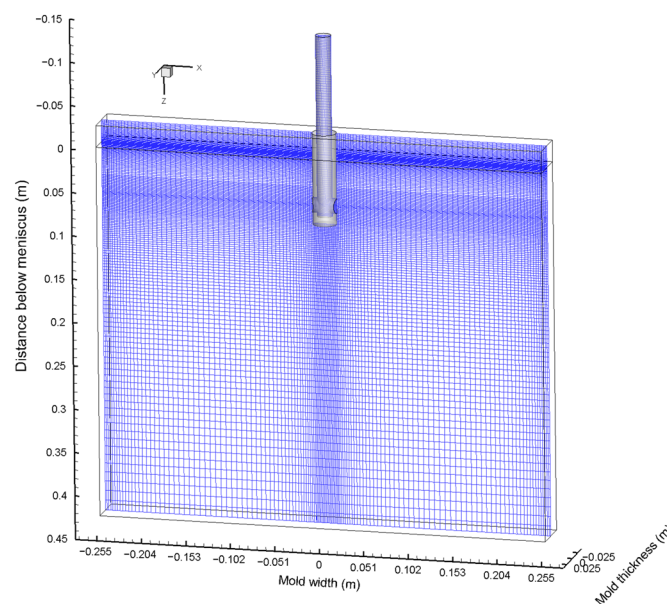

Figure 1. Schematic diagram of the computational domain and mesh system.

2.3. Boundary Conditions

The constant velocity inlet boundary condition at the SEN inlet was used. The free-slip condition was used at the top of the mold, and the pressure outlet boundary condition was used at the outlet. The non-slip condition was adopted for other walls. The bubbles with an initial diameter of 0.71 mm (the measured average diameter of the water model) were injected at the inlet of the SEN. The bubbles were assumed to be removed when the volume fraction of the air was large than 0.5 and escaped at the outlet of the mold. The reflection condition was used for other walls.

3. Validation

The measured speed on the thickness centerline at 5 mm below the meniscus using Particle Image Velocimetry (PIV) was employed to validate the current mathematical model, as shown in Figure 2. The PIV is widely used to measure the velocity in water models. First, a certain number of small particles were added to the mold during the measurement. Then, a 532 nm laser was used to illuminate the measured flow field area, and the movement of the particles through multiple exposures was recorded. Finally, the particles were tracked, and the velocity distribution was calculated. The average diameter of the small particles was 15 μm, and the density of the particles was about 1.0. The predicted results were in good agreement with the measured results. The speed increased first and then decreased from the SEN to the narrow face. The maximum speed appeared near the 1/4 width of the mold.
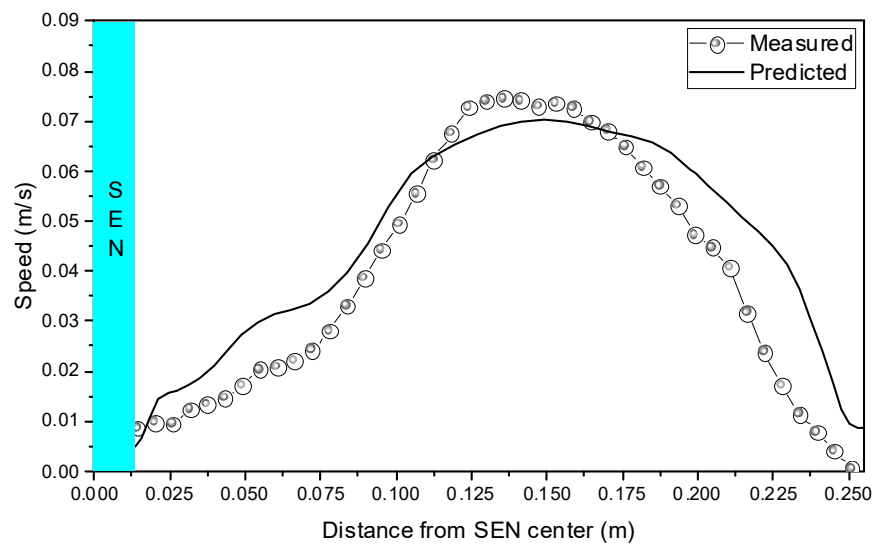
Figure 2. Comparison between the measured and the predicted result of the speed on the thickness centerline at 5 mm below the meniscus.

The space from the SEN to the narrow face was divided into 10 equal zones to count the distribution of bubbles. Figure 3 compares the measured and predicted distribution of the average diameter of the bubbles along the width of the mold. The difference between the predicted result and the measured result was small. The average bubble diameter was larger near the SEN, and the average bubble diameter decreased gradually from the SEN to the narrow face. The above results show that the current coupled LES turbulent model, VOF multiphase model, and DPM can accurately predict the multiphase flow and spatial distribution of the bubbles in the mold.
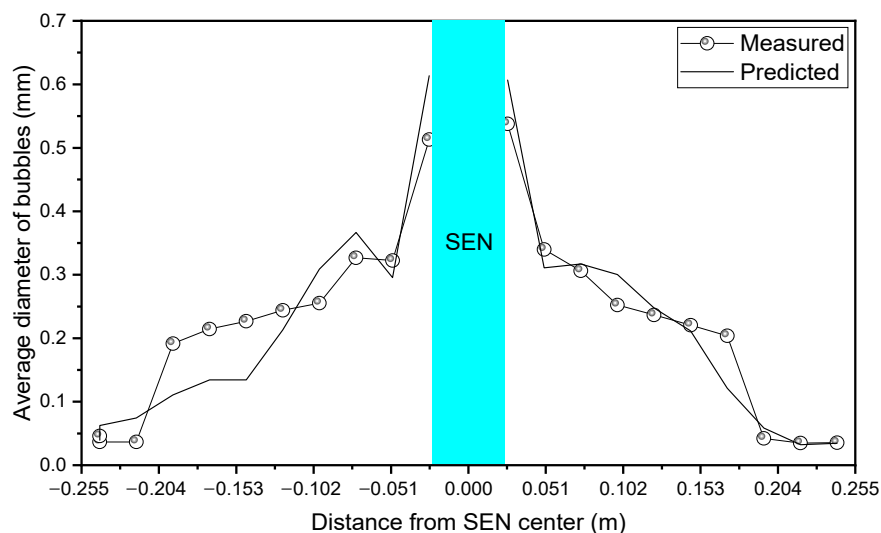

Figure 3. Comparison between the measured and the predicted result of the average bubble diameter along the width of the mold.

4. Results and Discussion

4.1. Distribution of the Transient Two-Phase Flow Field

The distribution of bubbles in the mold is mainly determined by the movement of the molten steel. Therefore, the correct simulation of the flow field is a prerequisite for predicting the distribution of the bubble size, number, and diameter. Figure 4 shows the distribution of the transient two-phase flow at different times. The current LES model successfully predicted the transient asymmetric two-phase flow in the mold. At t = 45 s,

the speed of the jet on the left side of the SEN was significantly higher than that on the right side. At t = 40 s and 50 s, the speed of the jet on both sides of the SEN was relatively consistent. However, the upper circulation speed at t = 40 s was significantly smaller than that at t = 50 s. When the casting speed and the gas flow rate were 0.425 m/min and 90 mL/min, respectively, the flow pattern in the mold was a typical double-roll flow.
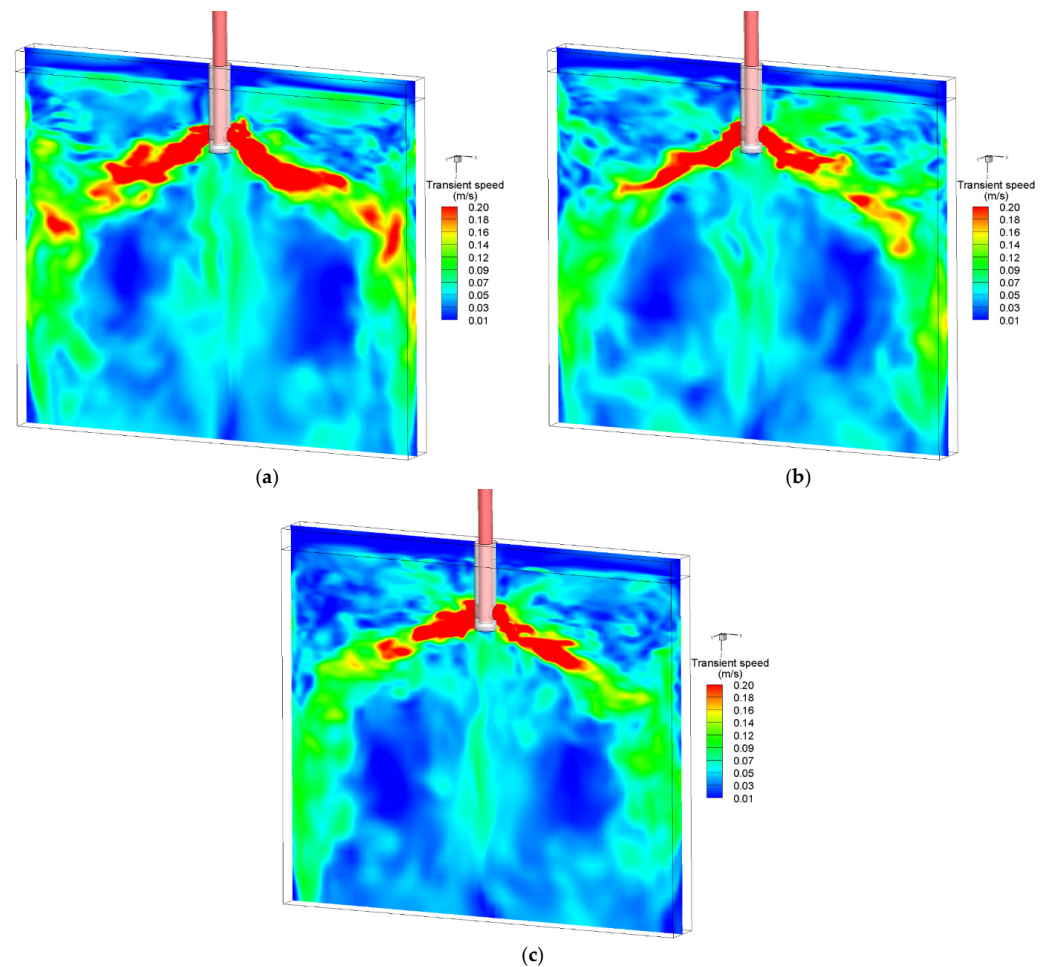

Figure 4. Distribution of the transient velocity at three different time shots: (**a**) t = 40.0 s; (**b**) t = 45.0 s; (**c**) t = 50.0 s.

Figure 5 shows the variation in the surface level over time near the narrow face, 1/4 width of the mold, and the SEN. The results show that the surface level near the narrow surface was the highest, and the surface level was the lowest near the 1/4 width of the mold. This is an inevitable result of the double-roll flow. The surface level near the narrow face was raised due to the lifting of the upper recirculation flow.

4.2. Spatial Distribution of the Bubbles

The collision of bubbles originated from the random movement of bubbles under turbulent flow. The different velocities between the bubbles make collisions between the bubbles possible. The outcome of the collision mainly included coalescence and bouncing. Figures 6 and 7 show the typical process of coalescence and bouncing of bubbles near the SEN, respectively. As shown in Figure 6a, the diameter of the bubble marked by the arrow was less than 2.34 mm. The bubbles then gradually collided and grew between 2.67 and 3.0 mm in Figure 6b and larger than 3.0 mm in Figure 6c. Figure 7a,c shows the complete process of the bounce of two bubbles. The current mathematical model considering the interaction between bubbles completely reproduced the movement of bubbles in molten steel and the phenomenon of bubble coalescence and bounce during the CC process.
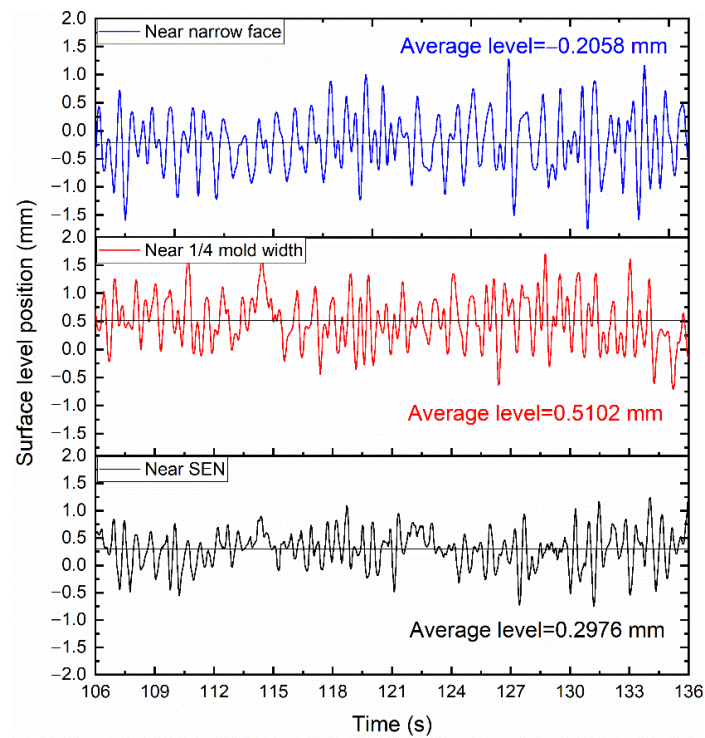
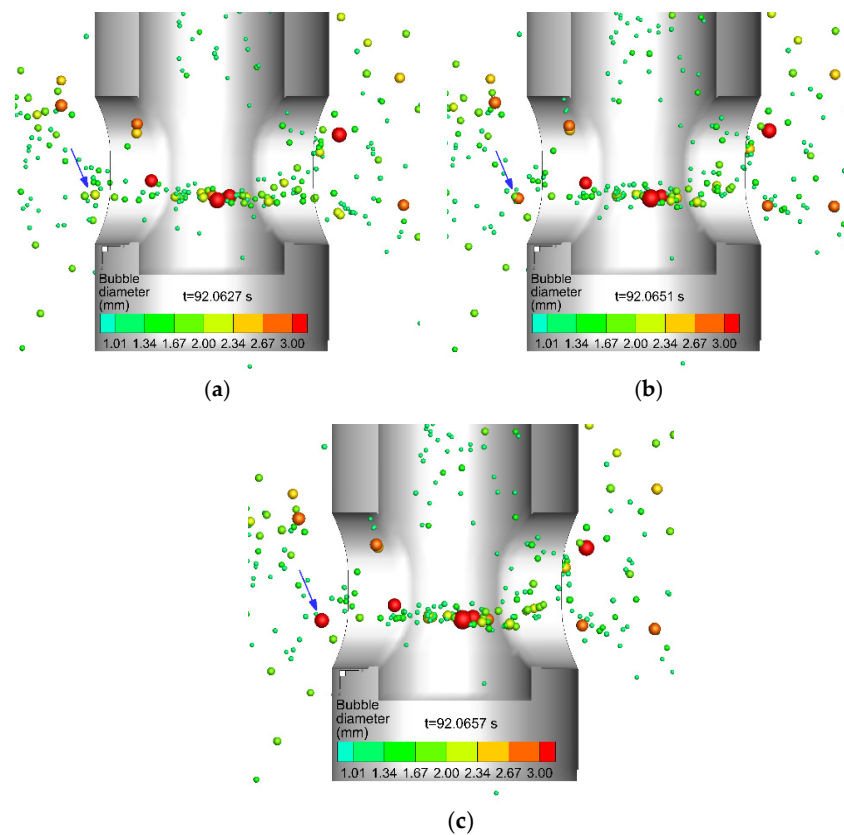**Figure 5.** The variation in surface level over time at different locations.

Figure 6. The typical process of the coalescence of bubbles (marked by a blue arrow), (**a**) t = 92.0627 s, (**b**) t = 92.0651 s, and (**c**) t = 92.0657 s.
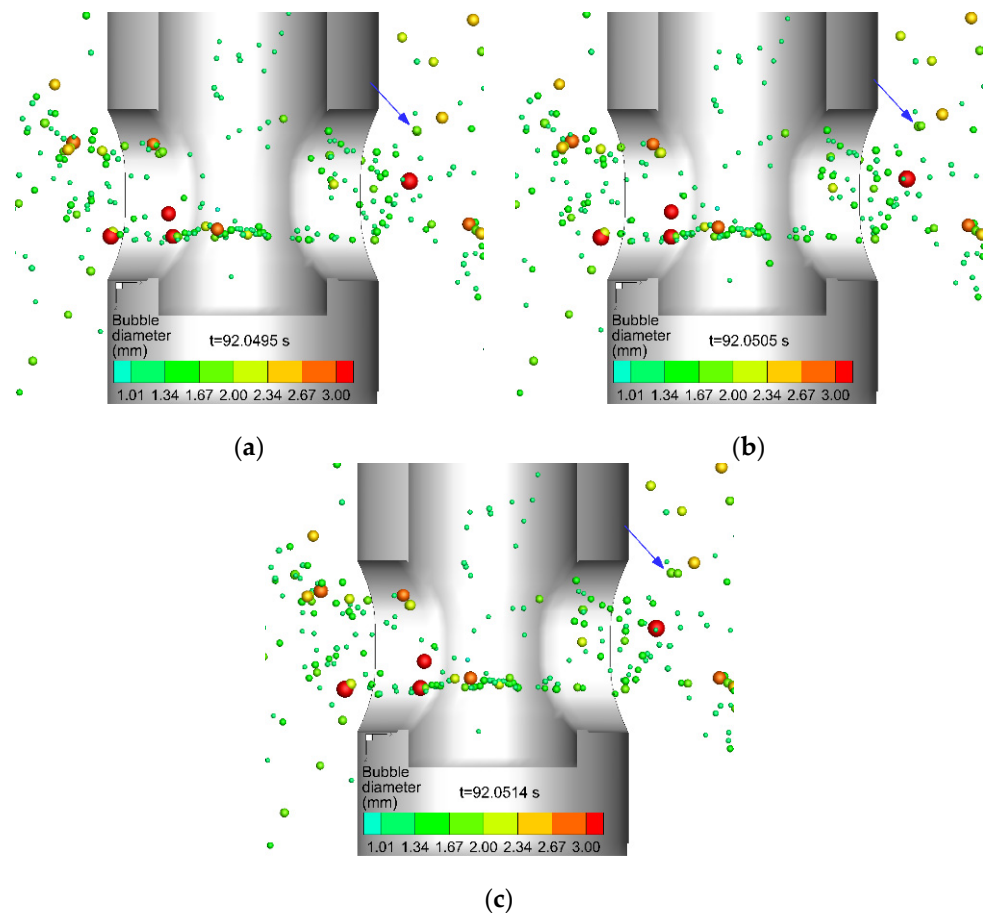
Figure 7. The typical process of the bounce of bubbles (marked by a blue arrow), (**a**) t = 92.0495 s, (**b**) t = 92.0505 s, and (**c**) t = 92.0514 s.

Figure 8 shows the typical process of the breakup of bubbles near the lower part of the SEN. The large bubble marked in Figure 8a was broken into small size bubbles in Figure 8b,c with the action of the fluid. In addition, some bubbles collided and grew larger. Breakup occurred when the diameter of the bubbles after coalescence exceeded the maximum diameter of the bubbles that could stably exist under the current turbulent energy dissipation rate. The strong turbulent motion of the molten steel after hitting the bottom of the SEN made the bubble breakup mainly occur near the bottom of the SEN. The breakup of bubbles was more likely to occur in the SEN region. The bubbles in the mold tended to collide.

Figure 9 shows the instantaneous spatial distribution of bubbles in the mold at t = 90 s. After the bubbles moved out of the SEN, the larger bubbles floated up near the SEN due to their greater buoyancy, while the small bubbles were distributed discretely in the entire mold with the action of the molten steel jet. Most of the bubbles floated up to the meniscus before reaching the narrow face, and overall, the bubbles were distributed in a fan shape. The distribution of bubbles in the mold was transient, including the bubble size, location, and number density. The bubbles collided and collapsed from an initial 0.71 mm into a multi-size distribution. The largest diameter exceeded 2 mm. The instantaneous spatial distribution of bubbles illustrated that the coalescence, bounce, and breakup of bubbles should be considered when predicting the two-phase flow and bubble distribution in the mold.
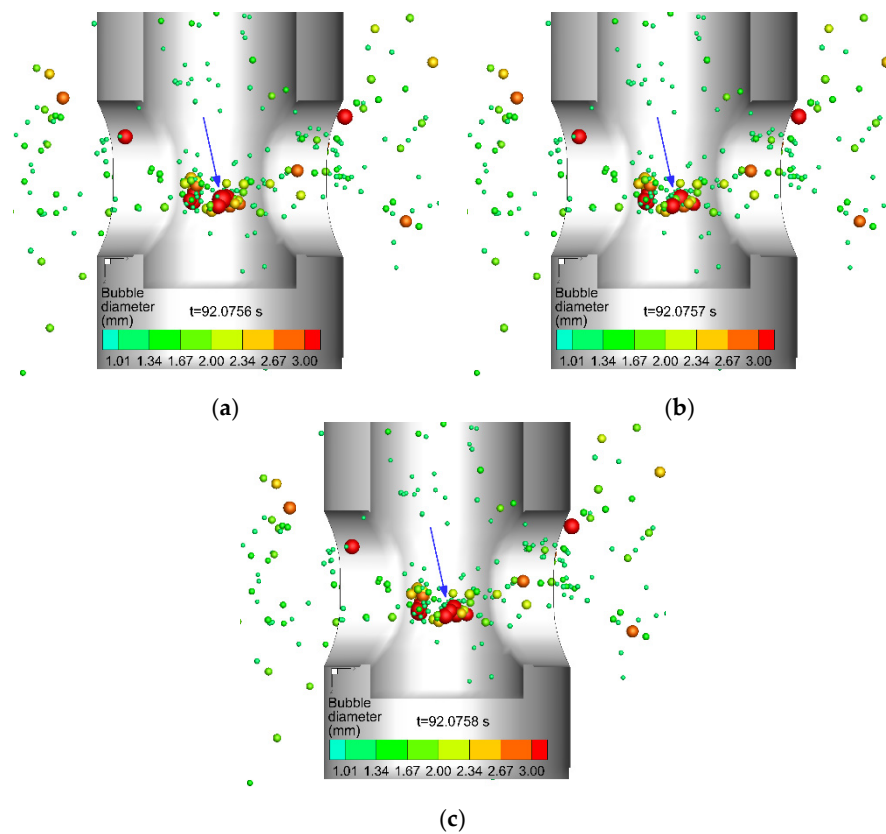
Figure 8. The typical process of the breakup of bubbles (marked by a blue arrow), (**a**) t = 92.0756 s, (**b**) t = 92.0757 s, and (**c**) t = 92.0758 s.
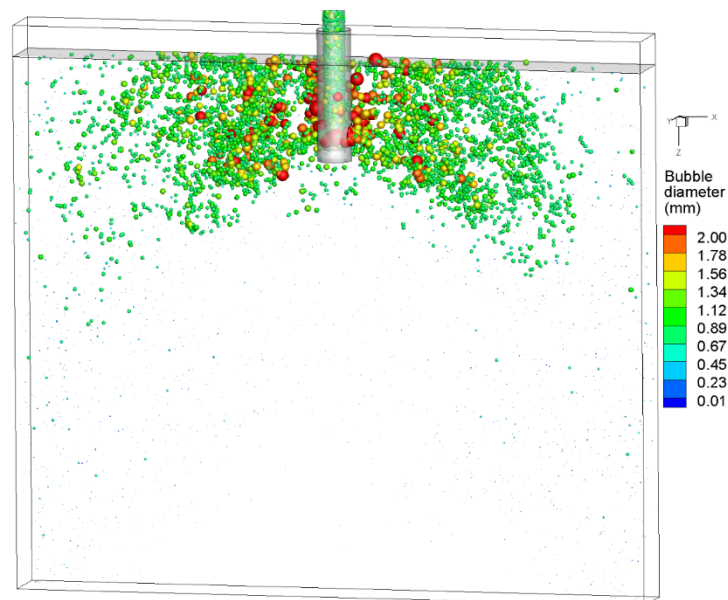

Figure 9. Spatial distribution of bubbles at t = 90 s.

Figure 10 shows the distribution of the average bubble concentration in the mold. The greatest average concentration of bubbles was in the lower part of the SEN and the upper edge of the SEN outlet. The drag force acting on the bubbles induced a relatively high bubble concentration in the jet region. In addition, the buoyancy of the larger bubbles increased the bubble concentration near the SEN. The large bubbles were broken up with the shearing of the molten steel to produce small bubbles distributed near the deep part of

the mold. These small bubbles brought into the deep part of the mold were easily captured by the solidified shell to form defects.
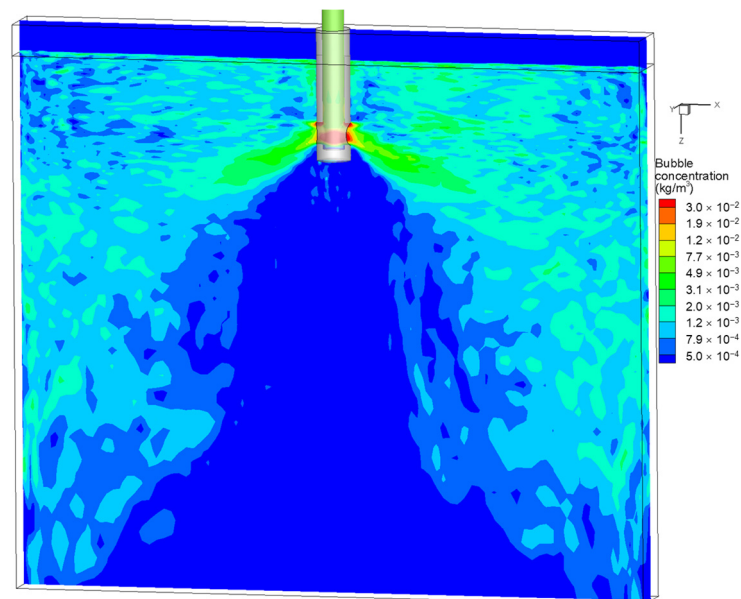

Figure 10. Distribution of the average bubble concentration in the mold.

5. Conclusions

In the current study, a three-dimensional mathematical model coupled with the LES turbulent model, the VOF multiphase model, and the DPM was developed to investigate the transient two-phase and spatial distribution of bubbles in a CC mold. The following conclusions were obtained:

1. The current mathematical model successfully predicted the transient asymmetric two-phase flow in the mold. The flow pattern in the mold was a typical double-roll flow with a 0.425 m/min casting speed and a 90 mL/min gas flow rate. The meniscus speed increased first and then decreased from the SEN to the narrow face, and the maximum speed appeared near the 1/4 width of the mold.
2. The interaction between the liquid and bubbles, and the coalescence, bounce, and breakup of bubbles, should be included to achieve an accurate prediction of the spatial distribution of bubbles.
3. Due to the violent movement of the fluid in the SEN, most of the breakup of the bubbles occurred in the SEN region. At the same time, the probability of the coalescence and bounce of bubbles in the SEN also increased. The bubbles in the mold tended to collide.
4. The bubbles collided and collapsed from an initial 0.71 mm into a multi-size distribution. The average bubble diameter was about 0.6 mm near the nozzle and gradually decreased to 0.05 mm from the nozzle to the narrow face. Most of the bubbles floated up to the meniscus before reaching the narrow face, and overall, the bubbles were distributed in a fan shape. The greatest average concentration of bubbles was in the lower part of the SEN and the upper edge of the SEN outlet.

Author Contributions: Conceptualization, Y.T., L.X., S.Q. and R.Z.; methodology, Y.T. and S.Q.; software, validation and writing—original draft preparation, Y.T.; formal analysis and visualization, Y.T. and P.S.; investigation, P.S.; resources and supervision, L.X., S.Q. and R.Z.; data curation, P.S.; writing—review and editing, L.X.; project administration and funding acquisition, S.Q. and R.Z. All authors have read and agreed to the published version of the manuscript.

Institutional Review Board Statement: Not applicable.

Informed Consent Statement: Not applicable.

Data Availability Statement: Not applicable.

Conflicts of Interest: The authors declare no conflict of interest.

References

1. Zhang, L.; Yang, S.; Cai, K.; Li, J.; Wan, X.; Thomas, B.G. Investigation of fluid flow and steel cleanliness in the continuous casting strand. *Metall. Mater. Trans. B* **2007**, *38*, 63–83. [CrossRef]
2. Jin, K.; Thomas, B.G.; Ruan, X. Modeling and measurements of multiphase flow and bubble entrapment in steel continuous casting. *Metall. Mater. Trans. B* **2016**, *47*, 548–565. [CrossRef]
3. Bai, H.; Thomas, B.G. Bubble formation during horizontal gas injection into downward-flowing liquid. *Metall. Mater. Trans. B* **2001**, *32*, 1143–1159. [CrossRef]
4. Lee, G.G.; Thomas, B.G.; Kim, S.H. Effect of refractory properties on initial bubble formation in continuous-casting nozzles. *Met. Mater. Int.* **2010**, *16*, 501–506. [CrossRef]
5. Liu, F.; Zhou, H.; Zhang, L.; Ren, C.; Zhang, J.; Ren, Y.; Chen, W. Effect of temperature and multichannel stopper rod on bubbles in water model of a steel continuous caster. *Steel Res. Int.* **2021**, *92*, 2100067. [CrossRef]
6. Ramos-Banderas, A.; Morales, R.; Sanchez-Perez, R.; Garcia-Demedices, L.; Solorio-Diaz, G. Dynamics of two-phase downwards flows in submerged entry nozzles and its influence on the two-phase flow in the mold. *Int. J. Multiph. Flow* **2005**, *31*, 643–665. [CrossRef]
7. Wang, Z.; Mukai, K.; Izu, D. Influence of wettability on the behavior of argon bubbles and fluid flow inside the nozzle and mold. *ISIJ Int.* **1999**, *39*, 154–163. [CrossRef]
8. Cho, S.M.; Thomas, B.G.; Kim, S.H. Bubble behavior and size distributions in stopper-rod nozzle and mold during continuous casting of steel slabs. *ISIJ Int.* **2018**, *58*, 1443–1452. [CrossRef]
9. Liu, Z.; Li, B.; Jiang, M.; Tsukihashi, F. Modeling of transient two-phase flow in a continuous casting mold using Euler-Euler large eddy simulation scheme. *ISIJ Int.* **2013**, *53*, 484–492. [CrossRef]
10. Yang, H.; Vanka, S.P.; Thomas, B.G. Mathematical modeling of multiphase flow in steel continuous casting. *ISIJ Int.* **2019**, *59*, 956–972. [CrossRef]
11. Pfeiler, C.; Wu, M.; Ludwig, A. Influence of argon gas bubbles and non-metallic inclusions on the flow behavior in steel continuous casting. *Mater. Sci. Eng. A* **2005**, *413*, 115–120. [CrossRef]
12. Toh, T.; Hasegawa, H.; Harada, H. Evaluation of multiphase phenomena in mold pool under in-mold electromagnetic stirring in steel continuous casting. *ISIJ Int.* **2001**, *41*, 1245–1251. [CrossRef]
13. Yu, H.; Zhu, M. Numerical simulation of the effects of electromagnetic brake and argon gas injection on the three-dimensional multiphase flow and heat transfer in slab continuous casting mold. *ISIJ Int.* **2008**, *48*, 584–591. [CrossRef]
14. Sanchez Perez, R.; García-Demedices, L.; Ramos, J.P.; Diaz Cruz, M.; Morales, R. Dynamics of coupled and uncoupled two-phase flows in a slab mold. *Metall. Mater. Trans. B* **2004**, *35*, 85–99. [CrossRef]
15. Sarkar, S.; Singh, V.; Ajmani, S.K.; Singh, R.K.; Chacko, E.Z. Effect of argon injection in meniscus flow and turbulence intensity distribution in continuous slab casting mold under the influence of double ruler magnetic field. *ISIJ Int.* **2018**, *58*, 68–77. [CrossRef]
16. Singh, V. Experimental simulation and mathematical modeling of air bubble movement in slab caster mold. *ISIJ Int.* **2006**, *46*, 210–218. [CrossRef]
17. Liu, Z.; Li, B. Large-eddy simulation of transient horizontal gas–liquid flow in continuous casting using dynamic subgrid-scale model. *Metall. Mater. Trans. B* **2017**, *48*, 1833–1849. [CrossRef]
18. Thomas, B.G.; Huang, X.; Sussman, R. Simulation of argon gas flow effects in a continuous slab caster. *Metall. Mater. Trans. B* **1994**, *25*, 527–547. [CrossRef]
19. Thomas, B.G. Review on modeling and simulation of continuous casting. *Steel Res. Int.* **2018**, *89*, 1700312. [CrossRef]
20. Ávila Ortiz, Y.; Morales, R.M.D.; Cedillo Hernández, V.; Delgado Pureco, J. Mathematical modeling of argon bubbling effects on fluid flow patterns of liquid steel in a slab mold. *Steel Res. Int.* **2018**, *89*, 1700453. [CrossRef]
21. Lopez, P.E.R.; Jalali, P.N.; Björkvall, J.; Sjöström, U.; Nilsson, C. Recent developments of a numerical model for continuous casting of steel: Model theory, setup and comparison to physical modelling with liquid metal. *ISIJ Int.* **2014**, *54*, 342–350. [CrossRef]
22. Lei, Z.; Chen, C.; Jin, X.; Zhong, Y.; Ren, Z. Numerical simulation of bubble behavior before inclined solidified front. *ISIJ Int.* **2013**, *53*, 830–837. [CrossRef]
23. Chen, W.; Ren, Y.; Zhang, L. Large eddy simulation on the two-phase flow in a water model of continuous casting strand with gas injection. *Steel Res. Int.* **2019**, *90*, 1800287. [CrossRef]
24. Chen, W.; Ren, Y.; Zhang, L.; Scheller, P.R. Numerical simulation of steel and argon gas two-phase flow in continuous casting using LES + VOF + DPM model. *JOM* **2019**, *71*, 1158–1168. [CrossRef]
25. Chen, W.; Zhang, L. Effects of interphase forces on multiphase flow and bubble distribution in continuous casting strands. *Metall. Mater. Trans. B* **2021**, *52*, 528–547. [CrossRef]

26. Chen, W.; Zhang, L.; Ren, Q.; Ren, Y.; Yang, W. Large eddy simulation on four-phase flow and slag entrainment in the slab continuous casting mold. *Metall. Mater. Trans. B* **2022**. [CrossRef]

27. Wang, Y.; Fang, Q.; Zhang, H.; Zhou, J.; Liu, C.; Ni, H. Effect of argon blowing rate on multiphase flow and initial solidification in a slab mold. *Metall. Mater. Trans. B* **2020**, *51*, 1088–1100. [CrossRef]

28. Liao, Y.; Lucas, D. A literature review on mechanisms and models for the coalescence process of fluid particles. *Chem. Eng. Sci.* **2010**, *65*, 2851–2864. [CrossRef]

29. Ribeiro, C.P., Jr.; Mewes, D. The effect of electrolytes on the critical velocity for bubble coalescence. *Chem. Eng. J.* **2007**, *126*, 23–33. [CrossRef]

30. Liao, Y.; Lucas, D. A literature review of theoretical models for drop and bubble breakup in turbulent dispersions. *Chem. Eng. Sci.* **2009**, *64*, 3389–3406. [CrossRef]

31. Nambiar, D.; Kumar, R.; Das, T.; Gandhi, K. A new model for the breakage frequency of drops in turbulent stirred dispersions. *Chem. Eng. Sci.* **1992**, *47*, 2989–3002. [CrossRef]

32. Liu, Z.; Qi, F.; Li, B.; Cheung, S.C.P. Modeling of bubble behaviors and size distribution in a slab continuous casting mold. *Int. J. Multiph. Flow* **2016**, *79*, 190–201. [CrossRef]

33. Santos, P.L., Jr.; Peixoto, J.J.M.; da Silva, C.A.; da Silva, I.A.; Galinari, C.M. Bubble behavior in the slab continuous casting mold: Physical and mathematical model. *J. Mater. Res. Technol.* **2020**, *9*, 4717–4726. [CrossRef]

34. Zhang, T.; Luo, Z.; Liu, C.; Zhou, H.; Zou, Z. A mathematical model considering the interaction of bubbles in continuous casting mold of steel. *Powder Technol.* **2015**, *273*, 154–164. [CrossRef]

35. Zhang, T.; Luo, Z.; Zhou, H.; Ni, B.; Zou, Z. Analysis of two-phase flow and bubbles behavior in a continuous casting mold using a mathematical model considering the interaction of bubbles. *ISIJ Int.* **2016**, *56*, 116–125. [CrossRef]

36. Yang, W.; Luo, Z.; Gu, Y.; Liu, Z.; Zou, Z. Simulation of bubbles behavior in steel continuous casting mold using an Euler-Lagrange framework with modified bubble coalescence and breakup models. *Powder Technol.* **2020**, *361*, 769–781. [CrossRef]

37. Yang, W.; Luo, Z.; Gu, Y.; Liu, Z.; Zou, Z. Numerical analysis of effect of operation conditions on bubble distribution in steel continuous casting mold with advanced bubble break-up and coalescence models. *ISIJ Int.* **2020**, *60*, 2234–2245. [CrossRef]

38. Yang, W.; Luo, Z.; Zhao, N.; Zou, Z. Numerical Analysis of Effect of Initial Bubble Size on Captured Bubble Distribution in Steel Continuous Casting Using Euler-Lagrange Approach Considering Bubble Coalescence and Breakup. *Metals* **2020**, *10*, 1160. [CrossRef]

39. Chaudhary, R.; Thomas, B.G.; Vanka, S.P. Effect of electromagnetic ruler braking (embr) on transient turbulent flow in continuous slab casting using large eddy simulations. *Metall. Mater. Trans. B* **2012**, *43*, 532–553. [CrossRef]

40. Real-Ramirez, C.A.; Carvajal-Mariscal, I.; Sanchez-Silva, F.; Cervantes-de-la-Torre, F.; Diaz-Montes, J.; Gonzalez-Trejo, J. Three-dimensional flow behavior inside the submerged entry nozzle. *Metall. Mater. Trans. B* **2018**, *49*, 1644–1657. [CrossRef]

41. Smagorinsky, J. General circulation experiments with the primitive equations: I. The basic experiment. *Mon. Weather Rev.* **1963**, *91*, 99–164. [CrossRef]

42. Tomiyama, A.; Tamai, H.; Zun, I.; Hosokawa, S. Transverse migration of single bubbles in simple shear flows. *Chem. Eng. Sci.* **2002**, *57*, 1849–1858. [CrossRef]

43. O'Rourke, P.J. *Collective Drop Effects on Vaporizing Liquid Sprays*; Princeton University: Princeton, NJ, USA, 1981.

44. Evans, G.; Jameson, G.; Atkinson, B. Prediction of the bubble size generated by a plunging liquid jet bubble column. *Chem. Eng. Sci.* **1992**, *47*, 3265–3272. [CrossRef]

45. Wang, T.; Wang, J.; Jin, Y. A novel theoretical breakup kernel function for bubbles/droplets in a turbulent flow. *Chem. Eng. Sci.* **2003**, *58*, 4629–4637. [CrossRef]

46. Kuboi, R.; Komasawa, I.; Otake, T. Collision and coalescence of dispersed drops in turbulent liquid flow. *J. Chem. Eng. Jpn.* **1972**, *5*, 423–424. [CrossRef]